Simulation and Experimental Study of Soil Behaviors under Principal Stress Rotations

Yunming Yang
Department of Civil Engineering, University of Nottingham Ningbo China, China

Yao Li
Department of Civil Engineering, University of Nottingham Ningbo China, China

Zhe Wang
Department of Civil Engineering, University of Nottingham Ningbo China, China

Hai-Sui Yu
Nottingham Centre for Geomechanics, University of Nottingham, UK

ABSTRACT: This paper presents an elastoplastic soil model considering the principal stress rotation (PSR) and an experimental facility associated with the PSR. The model is developed on the basis of a well-established kinematic hardening soil model using the bounding surface concept. The impact of the stress rate generating the PSR is treated independently, with its own hardening and flow rules. The new PSR model gives better simulations of soil behaviors under loading paths involving the PSR than the base model without special consideration of the PSR. A new experimental facility, Variable Direction Dynamic Cyclic Simple Shear (VDDCSS), manufactured by GDS is also introduced. It can independently exert two shear stresses to a soil specimen along two orthogonal directions. Test results indicate that directions of shear consolidation have a great impact on following undrained soil behaviors under both monotonic and cyclic shearing.

1 INTRODUCTION

Many types of loadings in geotechnical engineering can generate the principal stress rotation (PSR) in soil, such as the earthquake, wave and traffic loading (Ishihara & Towhata, 1983). Numerous experimental studies indicate that a change of principal stress directions, without a change of principal stress magnitudes, can lead to plastic deformations in soil (Miura et al, 1986; Gutierrez et al, 1991; Chen & Kutter, 2009). Further, the principal strain increment directions are not coincident with the principal stress directions under the PSR, and this non-coincidence is called the non-coaxiality. Neglecting the PSR induced deformations can lead to unsafe designs, such as in the study of sand liquefaction. In conventional elastoplastic theory, the stress rate generating the PSR and the non-PSR stress rate are not distinguished, so that the soil behavior can not be properly simulated under the loading including the PSR. A few elastoplastic constitutive models have been developed to treat the PSR stress rate and non-PSR stress rate separately (Gutierrez et al, 1991; Tsutsumi & Hashiguchi, 2005; Yang & Yu, 2006; Li & Dafalias, 2006). However, some of them can only properly simulate part of aspects involving the PSR, such as the non-coxiality. Some don't properly define and separate the PSR stress rate. Some can only be used in monotonic loading. Some are complicated and not easy to be numerically implemented. This paper aims to develop a soil model which can properly reproduce all characteristics of soil re-

sponses induced by the PSR in a relatively concise way. For this purpose, a well-established kinematic hardening soil model with the bounding surface concept is used as a base model (Dafalias & Manzari, 2004).

Loading paths involving the PSR can be complicated in geotechnical engineering practice (Boulanger & Seed, 1995; DeGroot et al, 1996). For instance, the direction of shear consolidation is very often different from following dynamic shear direction. Other complicated PSR loading paths can be in the form of oval shape or shape '8'. They are associated with exerting shear stresses to a soil sample along two orthogonal directions. For this purpose, the GDS manufactured an experimental facility, Variable Direction Dynamic Cyclic Simple Shear (VDDCSS), which can independently apply two shear stresses to a soil specimen along two orthogonal directions. The first set of test results by using the equipment are presented, concerning the impact of different directions of shear consolidation on following undrained soil behaviors under monotonic and cyclic shearing.

2 THE ORIGINAL BASE MODEL

The total strain rate $d\varepsilon$ can be broken down into the elastic $d\varepsilon^e$ and plastic component $d\varepsilon^p$, which is composed of $d\varepsilon_m^p$ from the stress rate without the PSR $d\sigma_m$, named as the monotonic loading for simplicity, and the $d\varepsilon_r^p$ from the PSR $d\sigma_r$. The sub-

script m and r represent the monotonic loading and PSR loading hereafter, respectively. $d\boldsymbol{\varepsilon}^e$ and $d\boldsymbol{\varepsilon}_m^p$ can be obtained by using the conventional elasto-plasticity theory. A well-established soil model with the kinematic hardening and bounding surface concept is used (Dafalias & Manzari, 2004) as the base model, which doesn't consider the PSR. Its formulations are briefly presented in this section, and the details can be found in Dafalias & Manzari (2004). The yield function of model is,

$$f = [(\mathbf{s} - p\boldsymbol{\alpha}):(\mathbf{s} - p\boldsymbol{\alpha})]^{1/2} - \sqrt{2/3}\,pm = 0 \quad (1)$$

where $\mathbf{s}$ and p are deviatoric stress tensor and confining pressure, respectively. $\boldsymbol{\alpha}$ is the back-stress ratio representing the center of yield surface, and m is the radius of yield surface on the deviatoric plane with a very small constant. $d\boldsymbol{\varepsilon}_m^p$ is given as,

$$d\boldsymbol{\varepsilon}_m^p = \langle L_m \rangle \mathbf{R}_m = \frac{1}{K_{pm}}(\frac{\partial f}{\partial \boldsymbol{\sigma}} d\boldsymbol{\sigma}_m)\mathbf{R}_m \quad (2)$$

where L_m represents the loading index, K_{pm} is the plastic modulus and $\mathbf{R}_m$ represents the flow direction. K_{pm} is defined as,

$$K_{pm} = \frac{2}{3}p\left[G_0 h_0(1 - c_h e)\left(\frac{p}{p_{at}}\right)^{-1/2}\right]\left[\frac{|\mathbf{b}:\mathbf{n}|}{|(\boldsymbol{\alpha} - \boldsymbol{\alpha}_{in}):\mathbf{n}|}\right] \quad (3)$$

where $\mathbf{b}$ is the distance between the current back-stress ratio tensor and bounding back-stress ratio tensor on the bounding surface. G_0, h_0 and c_h are the plastic modulus model parameters. $\mathbf{R}_m$ is defined as,

$$\mathbf{R}_m = \mathbf{n} + \frac{1}{3}D_m\mathbf{I} = \mathbf{n} + \frac{1}{3}A_d(\mathbf{d}:\mathbf{n})\mathbf{I} \quad (4)$$

where $\mathbf{n}$ represents the normal to the yield surface on the deviatoric plane, and D_m is the dilatancy ratio. $\mathbf{d}$ is the distance between the current back-stress ratio tensor and dilatancy back-stress ratio tensor, and A_d is a dilatancy model parameter.

The model is first used to predict stress-strain responses of Toyoura sand under drained conditions, in which several typical stress paths are studied. One is the monotonic loading paths (F paths) in which monotonic loadings are applied at different angles with the horizontal bedding plane (Miura et al, 1986). This is also used to calibrate model parameters. Another loading path is the pure PSR path (R paths), in which the stress ratio $(\sigma_a - \sigma_t)/(\sigma_a + \sigma_t)$ is chosen to be 0.5 (R1) and 0.6 (R2), respectively (Miura et al, 1986). In all those tests, the confining pressure remains constant at 98 kPa, and b remains constant at 0.5. Figure 1 shows the tests results and model predictions for the monotonic tests, and a reasonably good agreement is achieved. It is noted that this model doesn't consider the role of fabric anisotropy, and its simulations are intended to fit the average of all tests results along different loading directions. Table 1 shows the model parameters calibrated in the monotonic loading test.

Figure 2 shows the responses of various strain components including the volumetric strain with ro-tational angles of principal stress in tests results and predictions for the PSR path R1. Figure 3 shows the tests results and predictions for the PSR path R2, starting at $2\alpha = 180^0$. Figure 2 shows a reasonably good agreement between the test results and predictions in the PSR path R1, except for the radial strain, which is much smaller than other strain components and can be neglected. However, Figure 3 shows the discrepancy between the predicted and measured results is much larger in R2 than in R1, especially for the shear strain and volumetric strain. The predicted volumetric strain is much smaller than that measured in the test.

Table 1. Model parameters in the original and modified models for Toyoura sand (the first line) and Nevada sand (the second line)

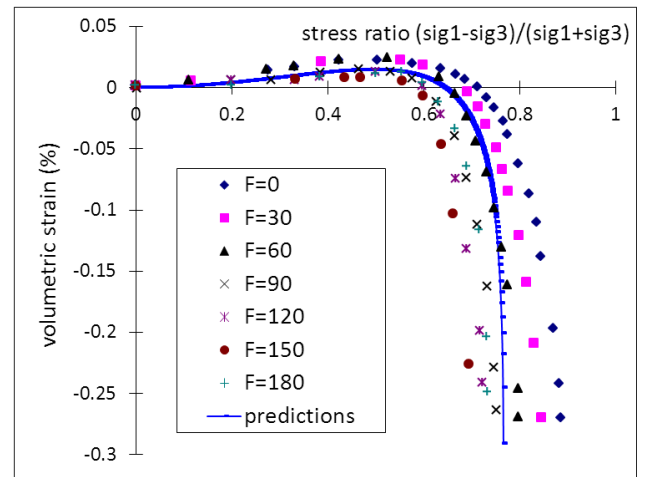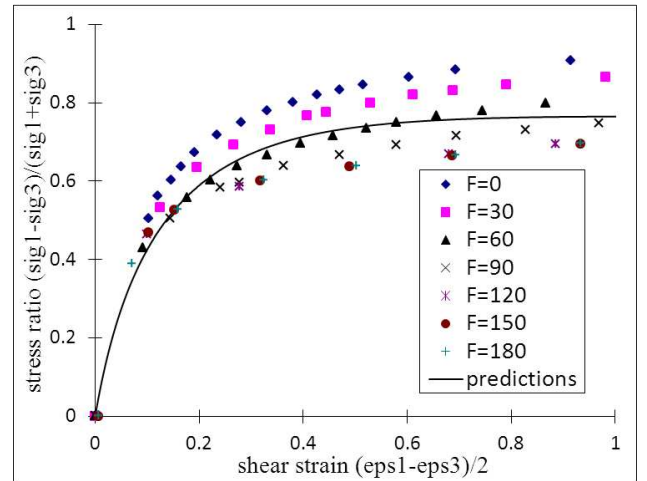| original model							
elasticity		critical state					Y.S.
G_0	v	M	c	λ_c	e_0	ξ	m
125	0.25	1.25	0.712	0.019	0.934	0.7	0.01
150	0.2	1.45	0.689	0.0052	0.807	0.5	0.01
plasticity			dilatancy		modified model		
h_0	c_h	n^b	A_0	n^d	h_{0r}	ξ^r	A_r
15	0.968	1.1	0.8	0.9	10	1.5	0.4
5.5	0.968	0.55	0.6	3.5	0.9	1.1	0.18

Figure 1. Test results and model predictions of the monotonic loadings in Miura et al (1986) for Toyoura sand (F denotes the angle of loading).

It is because the stress ratio in R2 is close to dilatancy surface or the phase transformation line, which results in a smaller predicted volumetric contraction. If the PSR occurs at a stress ratio a little higher than that in R2 or above the phase transformation line ($(\sigma_a - \sigma_t)/(\sigma_a + \sigma_t) = 0.65$), the volumetric expansion is even generated in simulations, which is shown in Figure 3. The poor prediction of volumetric strain has a serious consequence in the study of undrained soil behaviors in which the plastic volumetric strain directly controls the generation of pore water pressures. The discrepancy is understandable as the model doesn't distinguish the PSR and non-PSR stress rate, and all the model parameters are calibrated in the monotonic loadings.
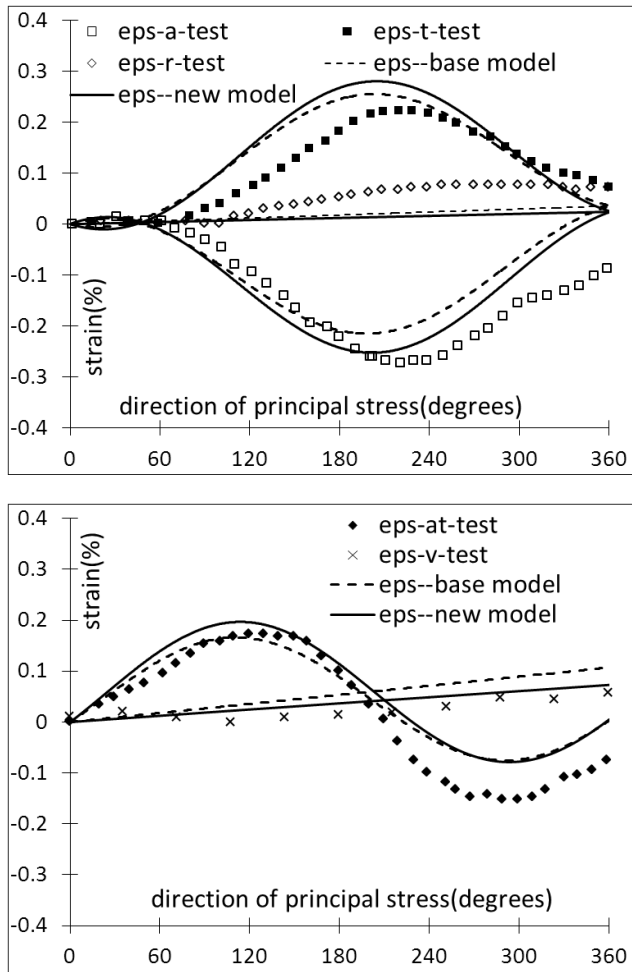

Figure 2. Test results and predictions of PSR loadings R1 in Miura et al (1986) with the original base model and the modified new model (eps-a: axial strain; eps-t: circumferential strain; eps-r: radial strain; eps-at: shear strain; eps-v: volumetric strain).

The model is also used to reproduce stress-strain responses of Nevada sand with three stress paths in hollow cylinder tests. The first one is the drained triaxial compression with various initial confining pressures and relative densities. In the second path called the torsional shear, the soil specimen is first subjected to drained triaxial extension loading with $K_0 = 1.38$, followed by a cyclic loading of shear stress

under undrained conditions until liquefaction occurs. Because the loading starts with the initial anisotropic condition and the effective confining pressure can't reach zero, and the liquefactions manifest themselves through large deformations. In the third path called the rotational shear, the soil is subjected to continuous principal stress rotations under undrained conditions. Figure 4 shows typical test results and simulations under triaxial compressions, and they are used to calibrate model parameters, shown in Table 1. Figures 5 and 6 show the test results and model simulations under the second and third stress paths. These two figures indicate that the model predictions are unable to bring the soil to liquefactions.
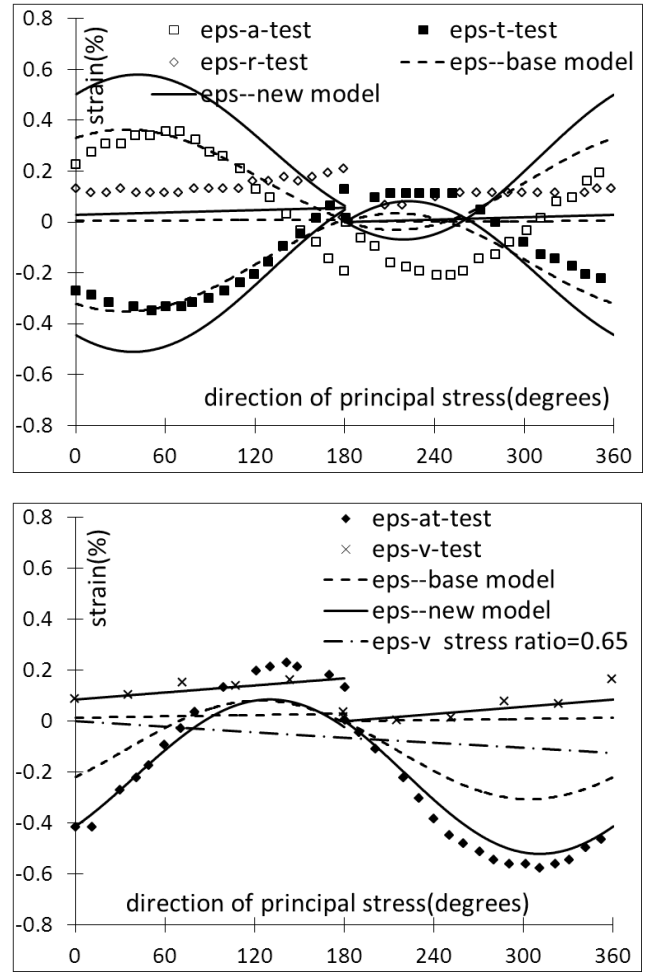

Figure 3. Test results and predictions of PSR loadings R2 in Miura et al (1986) and the volumetric strain for the additional stress ratio (0.65) with the original base model and the modified new model

3 THE MODIFIED MODEL WITH THE PSR

In the modified model, the stress rate component generating the PSR is treated independently. One can refer to Yang & Yu (2013) for detailed descriptions, and a brief description is presented in this section. $d\boldsymbol{\varepsilon}_r^p$ generated from $d\boldsymbol{\sigma}_r$ is given as,

$$d\boldsymbol{\varepsilon}_r^p = \langle L_r \rangle \mathbf{R}_r = \frac{1}{K_{pr}}(\frac{\partial f}{\partial \boldsymbol{\sigma}} d\boldsymbol{\sigma}_r)\mathbf{R}_r \tag{5}$$

$$K_{pr} = \frac{2}{3} p \left[G_0 h_{0r} (1 - c_h e) \left(\frac{p}{p_{at}} \right)^{-1/2} \right] \left(\frac{|\mathbf{b}:\mathbf{n}|}{|(\boldsymbol{\alpha} - \boldsymbol{\alpha}_{in}):\mathbf{n}|} \right)^{\xi_r} \quad (6)$$

where L_r is the loading index, K_{pr} plastic modulus and $\mathbf{R}_r$ flow direction from the PSR. h_{0r} and ξ_r are new model parameters for the PSR plastic modulus. The PSR plastic modulus is similar to that for the monotonic loading except the addition of ξ_r. ξ_r is generally larger than unity, which makes K_{pr} more sensitive to the stress ratio. $\mathbf{R}_r$ is defined as,

$$\mathbf{R}_r = \mathbf{n}_r + \frac{1}{3} D_r \mathbf{I} = \mathbf{n}_r + \frac{1}{3} A_r \left(\mathbf{1} - \frac{\alpha}{\alpha_\theta^b} \right) \mathbf{I} \quad (7)$$

where D_r is the dilatancy ratio, and A_r is the dilatancy model parameter for the PSR loading. α and α_θ^b are the amplitudes of back-stress ratio and bounding back-stress ratio. $\mathbf{n}_r$ can be approximated to be $\mathbf{n}$ in many cases. The determination of D_r uses the postulate for the PSR dilatancy rule by Gutierrez et al (1991). Thus, three new PSR related model parameters are used in the modified model. They are independent of the monotonic loading, and can be easily obtained through pure PSR loading paths at different stress ratio levels.

The final task is to determine $d\boldsymbol{\sigma}_r$. It is first determined in two dimension (x, y), denoted with α. It can be expressed as $d\boldsymbol{\sigma}_r^\alpha = \mathbf{N}_r^\alpha d\boldsymbol{\sigma}$, written in a matrix form as,

$$\begin{pmatrix} d\sigma_{rx}^\alpha \\ d\sigma_{ry}^\alpha \\ d\sigma_{rxy}^\alpha \end{pmatrix} = \begin{bmatrix} \frac{1}{2} - \frac{(\sigma_x - \sigma_y)^2}{8t_J^\alpha} & -\frac{1}{2} + \frac{(\sigma_x - \sigma_y)^2}{8t_J^\alpha} & -\frac{(\sigma_x - \sigma_y)\sigma_{xy}}{2t_J^\alpha} \\ -\frac{1}{2} + \frac{(\sigma_x - \sigma_y)^2}{8t_J^\alpha} & \frac{1}{2} - \frac{(\sigma_x - \sigma_y)^2}{8t_J^\alpha} & \frac{(\sigma_x - \sigma_y)\sigma_{xy}}{2t_J^\alpha} \\ -\frac{(\sigma_x - \sigma_y)\sigma_{xy}}{4t_J^\alpha} & \frac{(\sigma_x - \sigma_y)\sigma_{xy}}{4t_J^\alpha} & 1 - \frac{\sigma_{xy}^2}{t_J^\alpha} \end{bmatrix} \begin{pmatrix} d\sigma_x \\ d\sigma_y \\ d\sigma_{xy} \end{pmatrix} \quad (8)$$

where $t_J^\alpha = (\sigma_x - \sigma_y)^2/4 + \sigma_{xy}^2$. Similarly, in the space (y, z) denoted with β and (z, x) with γ, they can be expressed as $d\boldsymbol{\sigma}_r^\beta = \mathbf{N}_r^\beta d\boldsymbol{\sigma}$ and $d\boldsymbol{\sigma}_r^\gamma = \mathbf{N}_r^\gamma d\boldsymbol{\sigma}$. Combining $d\boldsymbol{\sigma}_r^\alpha$, $d\boldsymbol{\sigma}_r^\beta$ and $d\boldsymbol{\sigma}_r^\gamma$, letting $d\sigma_{rx} = d\sigma_{rx}^\alpha + d\sigma_{rx}^\gamma$, $d\sigma_{ry} = d\sigma_{ry}^\alpha + d\sigma_{ry}^\beta$ and $d\sigma_{rz} = d\sigma_{rz}^\beta + d\sigma_{rz}^\gamma$, one can obtain $d\boldsymbol{\sigma}_r$ in the general stress space,

$$d\boldsymbol{\sigma}_r = \mathbf{N}_r d\boldsymbol{\sigma} \quad (9)$$
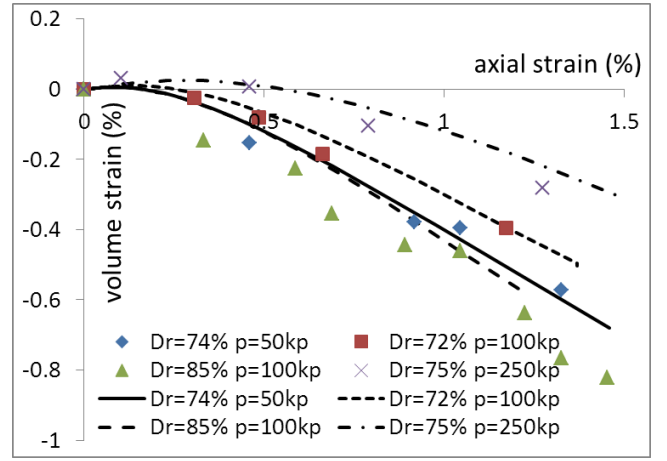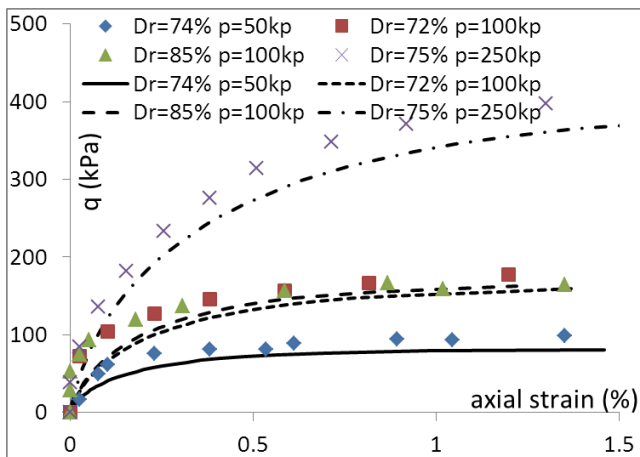

Figure 4. Test results and model predictions of the monotonic loadings in Chen & Kutter (2009) for Nevada sand

The total stress increment can be expressed as,

$$d\boldsymbol{\sigma} = \mathbf{E}(d\boldsymbol{\varepsilon} - d\boldsymbol{\varepsilon}^P) = \mathbf{E}(d\boldsymbol{\varepsilon} - d\boldsymbol{\varepsilon}_m^P - d\boldsymbol{\varepsilon}_r^P) \quad (10)$$

where $\mathbf{E}$ represents the elastic stiffness tensor. Using mathematical manipulations and the relationship

$$\mathbf{E}\mathbf{N}_r = 2G\mathbf{N}_r \quad (11)$$

One can obtain,

$$d\boldsymbol{\sigma} = \mathbf{E}^{ep} d\boldsymbol{\varepsilon} \quad (12)$$

$$\mathbf{E}^{ep} = \mathbf{E} - B_1 \left[\frac{(\mathbf{ER})(\mathbf{IN}_r^*)}{K_{pr} + \mathbf{IN}_r^* \mathbf{R}_r} - \frac{(\mathbf{ER})(\mathbf{IE})}{K_{pr} + \mathbf{IER}_r} \right] - B_2 \left[\frac{(\mathbf{ER}_r)(\mathbf{IN}_r^*)}{\mathbf{IN}_r^* \mathbf{R}} - \frac{(\mathbf{ER}_r)(\mathbf{IE})}{K_p + \mathbf{IER}} \right] \quad (13)$$

$$\mathbf{N}_r^* = 2G\mathbf{N}_r \quad (14)$$

$$B_1 = \left(\frac{\mathbf{IN}_r^* \mathbf{R}}{K_{pr} + \mathbf{IN}_r^* \mathbf{R}_r} - \frac{K_p + \mathbf{IER}}{K_{pr} + \mathbf{IER}_r} \right)^{-1} \quad (15)$$

$$B_2 = \left(\frac{K_{pr} + \mathbf{IN}_r^* \mathbf{R}_r}{\mathbf{IN}_r^* \mathbf{R}} - \frac{K_{pr} + \mathbf{IER}}{K_p + \mathbf{IER}} \right)^{-1} \quad (16)$$

These equations indicate that the stiffness tensor is independent of stress increments, and the stress and strain increments have a linear relationship. In these equations, if K_{pr} is set to be K_p and $\mathbf{R}_r$ to be $\mathbf{R}$, they will be downgraded to the formulations in the classical plasticity.
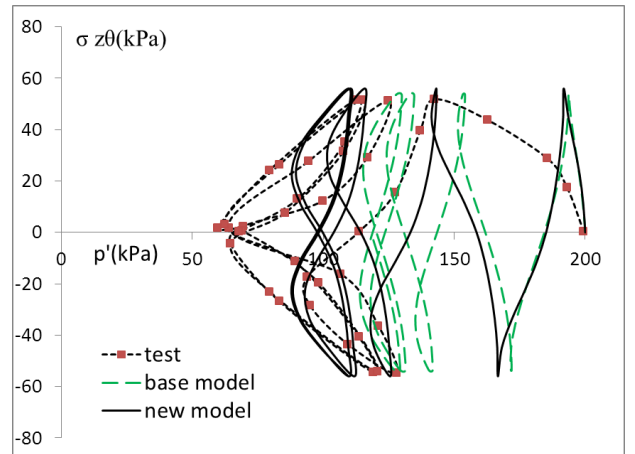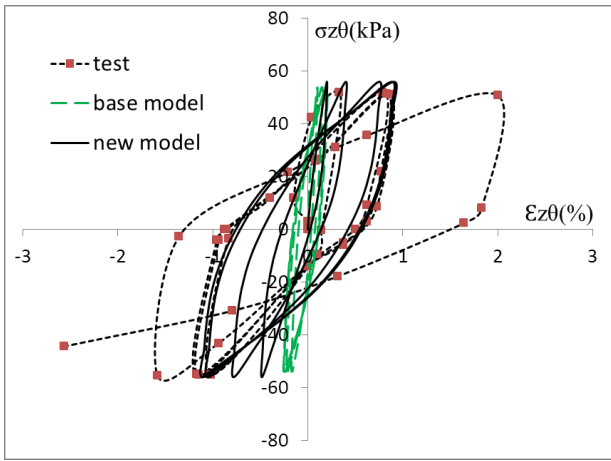
Figure 5. Test results and model predictions of the torsional shear tests in Chen & Kutter (2009)

Figures 2 and 3 show the drained predictions using the modified model for the tests in Miura et al (1986). These figures indicate that the new predictions have overall better agreements with the test results than the original predictions, especially for the shear and volumetric strains. Figures 5 and 6 show the new undrained predictions for Nevada sand, and they are able to reproduce the liquefaction, reflected by the large displacements.
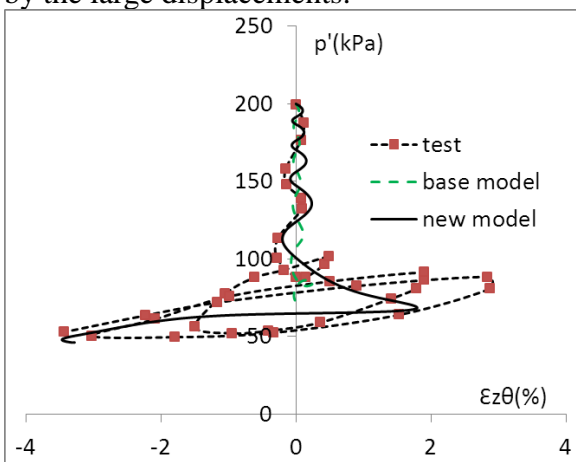

Figure 6. Test results and model predictions of the rotational shear tests in Chen & Kutter (2009)

4 EXPERIMENTAL STUDY

The Variable Direction Dynamic Cyclic Simple Shear (VDDCSS) manufactured by GDS is shown in Figure 7, in which there are three electro-mechanical actuators. The vertical actuator Z applies normal pressure to the specimen, and two orthogonal horizontal actuators X and Y independently apply two shear stresses. LVDT and motor encoders are used to measure displacements at three actuators. Cylindrical shaped soil samples with a diameter of 70mm and height of 17mm are used in tests. Teflon coated rings of 1mm height each are placed outside membrane of soil specimens. To test undrained soil responses, the height of soil specimens remain unchanged, and

change of vertical pressure on soil specimens are equivalent to the generation of pore water pressure. Leighton Buzzard sand (Fraction B) is used in all tests. The soil specimen is prepared by using dry deposition method, and consolidated under vertical pressure of 200 kPa. The relative density of soil is controlled near 75% after consolidation.

In the first series of tests, all specimens are sheared during consolidation with different angles to x direction, followed by undrained shear in x direction until soil failure, shown in Figure 7. The ratio of consolidation shear and initial vertical pressure (CSR) is 0.05 and 0.1, respectively. Figure 8 shows the response of shear stress and strain along x direction for the CSR of 0.1, together with the result without the consolidation shear. It indicates that a smaller angle leads to a larger peak and more brittle behavior. The angle of 0^0 has the most brittle behavior with the highest peak, and the angle of 180^0 has the most ductile behavior. The soil response with the angle of 90^0 and 120^0 don't reach the peak value because the soil fails along y direction. In the second series of tests, the specimen is sheared during consolidation to a CSR of 0.25 along 0^0 and 90^0 to x direction, followed by undrained cyclic shear of strain control with an amplitude of 0.24% along x direction. Figure 9 shows the response of shear strain-shear stress and development of pore water pressure-cycles of loading, together with the result without the consolidation shear. It indicates that the loading path with 90^0 leads to the fastest liquefaction, followed by that without the shear consolidation. The path with 0^0 has the slowest liquefaction. The results under the cyclic shearing are consistent with those under the monotonic loading, in which a smaller angle of consolidation shear increases the soil strength.

5 CONCLUSION

This paper first presents a soil model which can properly consider the impact of PSR on soil behaviors. The PSR generating stress rate is treated separately with its own hardening and flow rules. Model predictions indicate that the new model gives better reproduction of soil behaviors, especially the volumetric and shear strain responses. A new experimental facility VDDCSS is also introduced, which can exert shear stresses along two orthogonal directions. Test results indicate that the shear consolidation angle plays an important role on following monotonic and dynamic undrained shearing soil behaviors. A smaller angel generally leads to a higher strength and more brittle responses.

6 REFERENCES

Boulanger R.W. & Seed R.B. (1995), Liquefaction of sand under bidirectional monotonic and cyclic loading, Journal of geotechnical engineering, 121(12), 870-878

Chen, Y.R., Kutter, B.L. (2009), Contraction, dilation, and failure of sand in triaxial, torsional, and rotational shear tests, Journal of engineering mechanics, 135(10), 1155-1165

Dafalias, Y.F. & Manzari, M.T. (2004), Simple plasticity sand model accounting for fabric change effects, Journal of Engineering Mechanics, ASCE, 130(6), 622-634

DeGroot D.J., Ladd C.C. & Germaine J.T. (1996), Undrained multidirectional direct simple shear behavior of cohesive soil, Journal of geotechnical engineering, 122(2), 91-98

Gutierrez, M., Ishihara, K. & Towhata, I. (1991), Flow theory for sand during rotation of principal stress direction, Soils and foundations, 31(4), 121-132

Ishihara, K. & Towhata, I. (1983), Sand response to cyclic rotation of principal stress directions as induced by wave loads, Soils and Foundations, 23(4), 11-26

Li, X.S. & Dafalias, Y.F. (2004), A constitutive framework for anisotropic sand including non-proportional loading, Geotechnique, 54(1), 41-55

Miura, K., Miura, S. & Toki, S. (1986), Deformation behavior of anisotropic dense sand under principal stress axes rotation, Soils and Foundations, 26(1), 36-52

Tsutsumi, S. & Hashiguchi, K. (2005), General non-proportional loading behavior of soils, International Journal of Plasticity, 21, 1941-1969

Yang, Y. & Yu, H.S. (2006), A non-coaxial critical state model and its application to simple shear simulations, International Journal for Numerical and Analytical Methods in Geomechanics, 30, 1369-1390

Yang, Y. & Yu, H.S. (2013), A kinematic hardening soil model considering the principal stress rotation, International Journal for Numerical and Analytical Methods in Geomechanics, 37, 2106-2134
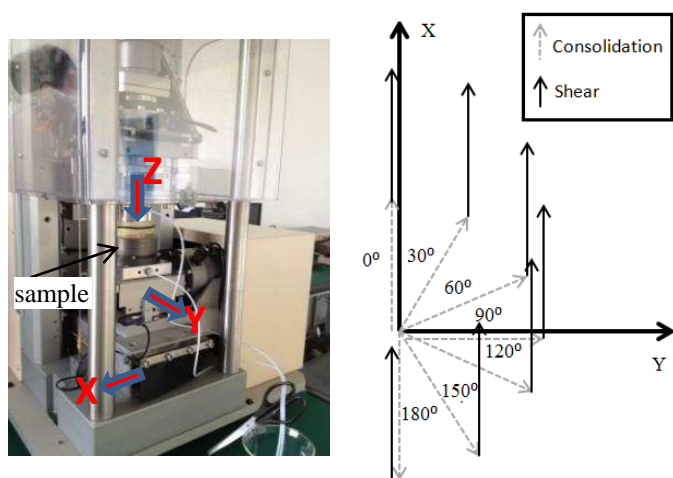
Figure 7. The VDDCSS and loading paths with consolidation shear followed by drained shear along different directions
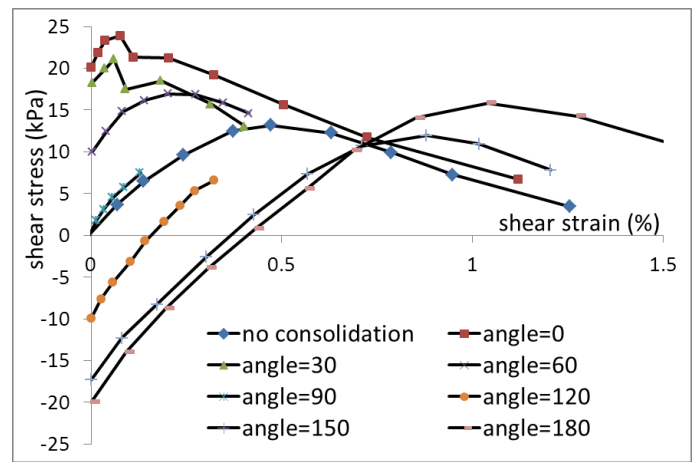

Figure 8. Test results for the loading paths with consolidation shear followed by undrained shear along different directions
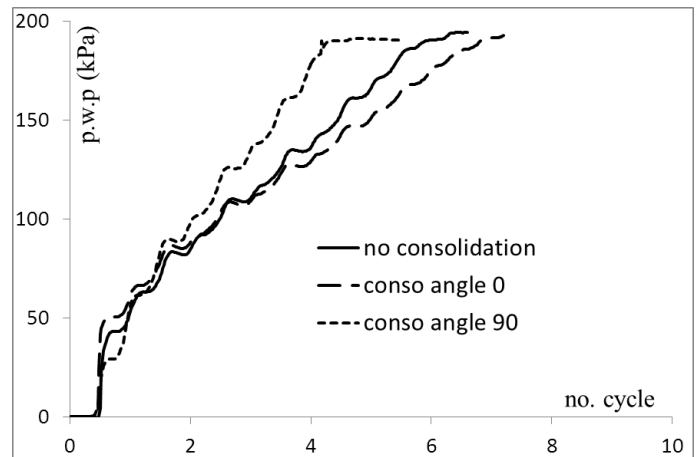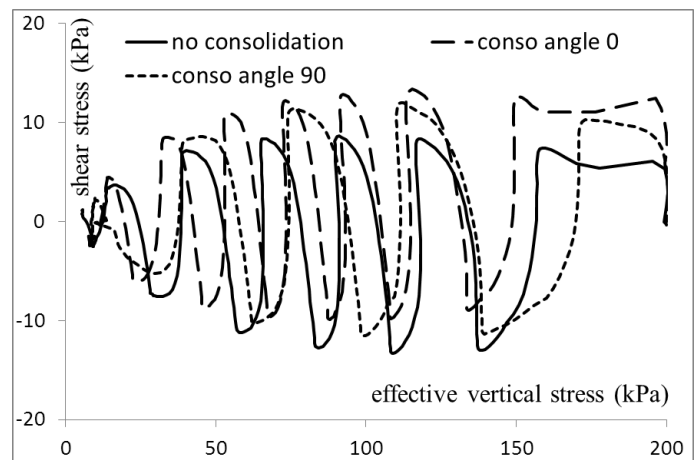

Figure 9. Test results for the loading paths with consolidation shear followed by undrained cyclic shear at different directions